Target-field design of surface permanent magnets

Peter J. Hobson, Chris Morley,[*] Alister Davis, Thomas Smith, and Mark Fromhold[†]
School of Physics & Astronomy, University of Nottingham, Nottingham NG7 2RD, United Kingdom

(Received 22 May 2024; revised 6 August 2024; accepted 12 August 2024; published 6 September 2024)

We present a target-field approach to analytically design magnetic fields using permanent magnets. We assume that their magnetization is bound to a two-dimensional surface and is composed of a complete basis of surface modes. By posing the Poisson's equation relating the magnetic scalar potential to the magnetization using Green's functions, we derive simple integrals that determine the magnetic field generated by each mode. This approach is demonstrated by deriving the governing integrals for optimizing axial magnetization on cylindrical and circular-planar surfaces. We approximate the governing integrals numerically and implement them into a regularized least-squares optimization routine to design permanent magnets that generate uniform axial and transverse target magnetic fields. The resulting uniform axial magnetic field profiles demonstrate more than a tenfold increase in uniformity across equivalent target regions compared to the field generated by an optimally separated axially magnetized pair of rings, as validated using finite element method simulations. We use a simple example to examine how two-dimensional surface magnetization profiles can be emulated using thin three-dimensional volumes and determine how many discrete intervals are required to accurately approximate a continuously varying surface pattern. Magnets designed using our approach may enable higher-quality bias fields for electric machines, nuclear fusion, fundamental physics, magnetic trapping, and beyond.

DOI: 10.1103/PhysRevApplied.22.034015

I. INTRODUCTION

Permanent magnets are materials containing iron, cobalt, or nickel that exhibit known stable magnetization, making them suited for generating static (dc) magnetic fields. The best permanent magnet materials, like ferrite ceramics and neodymium alloys, have a high retentivity, coercivity, and Curie temperature. Thus, their strong retained magnetization is resistant to being altered by external magnetic fields or temperature changes. Permanent magnets are extensively used in industrial applications to generate static magnetic fields in devices such as electric machines [1–5] and transducers [6,7]. Moreover, they are an essential component of many scientific experiments and apparatus that require strong static magnetic fields, including nuclear fusion stellerators [8–12], magnetic resonance imaging (MRI) scanners [13,14], Zeeman slowers [15,16], ion pumps [17,18], magnetic atom and ion traps [19,20], and electromagnetic isotope separators [21]. Specifically designed magnets that generate a strong field in one region and self-cancel so that the field is much weaker elsewhere, known as Halbach arrays [22], are applied extensively, particularly in focusing particle accelerator beams [23].

As such, the design of target magnetic field profiles using permanent magnets has garnered significant research interest. Roméo and Hoult's seminal paper [24] established methods for designing target magnetic field profiles by examining symmetries in the magnetic scalar potential and replicating them through the arrangement of simple magnetized structures such as loops and arcs. Drawing on their design principles, analytical models have been developed to create magnetized loops [25] and to study the Fourier series expansions of magnetic fields generated by hypothetical magnetic point charges [26]. Further analytical models have been developed to determine the optimal placement of magnetized rods [13,14] to enhance target-field profiles for low-power MRI applications. Alternatively, numerical methods have been developed to solve for the magnetic field generated by magnetized structures with more complex geometries, including surface pixels [27], surface meshes [8,11,12], and volumes [28]. While these approaches are very flexible, they provide limited insight into the physical behavior of permanent magnet systems and often demand extensive computations of integrals or

[*]Contact author: Christopher.Morley2@nottingham.ac.uk
[†]Contact author: Mark.Fromhold@nottingham.ac.uk

at numerous evaluation points to find precise solutions. Consequently, design optimization often has a limited resolution and is computationally intensive, restricting the potential for design refinement.

In contrast, when designing current-carrying magnetic field coils, rather than permanent magnets, complex surface patterns may be designed straightforwardly and efficiently using a family of approaches known as *target-field methods*, conceived initially by Turner [29]. Target-field methods use Green's function solutions to express the magnetic field in terms of Fourier space integrals, with the Fourier transform of surface current flow modes included in the integral argument. By selecting suitable surface flows in an orthogonal basis, typically a Fourier series with symmetries that match those in the Green function, these integrals can be solved analytically or converge efficiently numerically [30–32]. Quadratic optimization methods, commonly least-squares optimization, can then be used to determine the weights of different current flow modes to achieve the desired target-field [33]. These current flows may oscillate greatly across the surface to control magnetic field variations and thereby enhance magnetic field fidelity over a target region.

In this paper, we extend the target-field method approaches used for designing current flows to the analytic design of surface magnetization. This enables us to optimize complicated target profiles using complex magnetization arrangements efficiently and straightforwardly. We begin by employing cylindrical Green functions to derive Fourier space integrals that relate axial magnetization on cylindrical or circular-planar surfaces to the magnetic field via the magnetic scalar potential. We then introduce Fourier series representations of axial magnetization on these surfaces and input these series representations into the Fourier space integrals. We numerically solve these integrals to design surface magnetization on cylindrical and circular biplanar surfaces through least-squares optimization, regularized by the curvature across the surface of the magnet. These surface magnetization patterns therefore generate uniform axial and transverse magnetic fields, but without excessive spatial oscillations across their surfaces that would increase manufacturing complexity. The magnetic field profiles created by these surface patterns are validated by comparison to finite element method (FEM) simulations, which show strong agreement with theoretical predictions. We also propose approaches to replicate the two-dimensional (2D) surface magnetization profiles with patterns that can be produced using sets of thin 3D magnetized regions with incrementally increasing surface magnetization, such as stacks of equally thin magnetized metal plates. We use a simple example to assess how the thickness of a 3D volume and the number of discrete magnetized regions influences the quality of the generated magnetic field.

II. MATHEMATICAL MODEL

A. Green's function formulation

Let us consider a region of space containing no electrical currents and only permanent magnets with a fixed magnetization, $\mathbf{M}$, such that the magnetic flux density, outside the magnets, in free space, is $\mathbf{B} = \mu_0(\mathbf{H} + \mathbf{M})$, where $\mathbf{H}$ is the magnetic field strength and μ_0 is the magnetic permeability of free space. In this scenario, the magnetic flux density in free space is simply the gradient of the magnetic scalar potential,

$$\mathbf{B}(\mathbf{r}) = -\mu_0 \nabla_{\mathbf{r}} \Psi(\mathbf{r}), \tag{1}$$

where the magnetic scalar potential is evaluated at a point $\mathbf{r} = x\,\hat{\mathbf{x}} + y\,\hat{\mathbf{y}} + z\,\hat{\mathbf{z}}$ and $\nabla_{\mathbf{r}} = (\partial/\partial x)\hat{\mathbf{x}} + (\partial/\partial y)\hat{\mathbf{y}} + (\partial/\partial z)\hat{\mathbf{z}}$.

Applying Ampère's law, $\nabla \times \mathbf{H} = 0$, and Gauss' law of magnetism, $\nabla \cdot \mathbf{H} = -\nabla \cdot \mathbf{M}$, then inputting the magnetic scalar potential, (1), we can generate the following Poisson equation for the magnetic scalar potential in free space:

$$\nabla^2_{\mathbf{r}} \Psi(\mathbf{r}) = \nabla_{\mathbf{r}} \cdot \mathbf{M}(\mathbf{r}). \tag{2}$$

Defining a Green's function as $\nabla^2_{\mathbf{r}} G(\mathbf{r}, \mathbf{r}') = \delta(\mathbf{r} - \mathbf{r}')$, where $\delta(x)$ is the Dirac delta function, we can integrate Eq. (2) to find that [34]

$$\Psi(\mathbf{r}) = -\frac{1}{4\pi} \int d\mathbf{r}'\, \nabla_{\mathbf{r}} \cdot \left(\frac{\mathbf{M}(\mathbf{r}')}{|\mathbf{r} - \mathbf{r}'|} \right), \tag{3}$$

where Green's function is now represented as $G(\mathbf{r}, \mathbf{r}') = 1/|\mathbf{r} - \mathbf{r}'|$ and $\mathbf{r}' = x'\hat{\mathbf{x}} + y'\hat{\mathbf{y}} + z'\hat{\mathbf{z}}$ is a point within the magnetized region.

Let us now apply the vector identity

$$\nabla_{\mathbf{r}} \cdot \left(\frac{\mathbf{M}(\mathbf{r}')}{|\mathbf{r} - \mathbf{r}'|} \right) = \frac{1}{|\mathbf{r} - \mathbf{r}'|} \nabla_{\mathbf{r}} \cdot \mathbf{M}(\mathbf{r}') + \mathbf{M}(\mathbf{r}') \nabla_{\mathbf{r}} \cdot \left(\frac{1}{|\mathbf{r} - \mathbf{r}'|} \right), \tag{4}$$

and note that the divergence of the magnetization must be zero outside of the magnetized region, $\nabla_{\mathbf{r}} \cdot \mathbf{M}(\mathbf{r}') = 0$. Substituting Eq. (4) into Eq. (3), we generate an integral representation of the magnetic scalar potential,

$$\Psi(\mathbf{r}) = -\frac{1}{4\pi} \int d\mathbf{r}'\, \mathbf{M}(\mathbf{r}') \nabla_{\mathbf{r}} \cdot \left(\frac{1}{|\mathbf{r} - \mathbf{r}'|} \right). \tag{5}$$

By imposing that the magnetization is directed only along the axial direction, $\mathbf{M} = M_z \hat{\mathbf{z}}$, this simplifies further to

$$\Psi(\mathbf{r}) = -\frac{1}{4\pi} \int d\mathbf{r}'\, M_z(\mathbf{r}') \frac{\partial}{\partial z} \left(\frac{1}{|\mathbf{r} - \mathbf{r}'|} \right). \tag{6}$$

Below, we match the spatial symmetries of the surface upon which we wish to design magnetization to an appropriate Green's function, and thereby simplify the integral

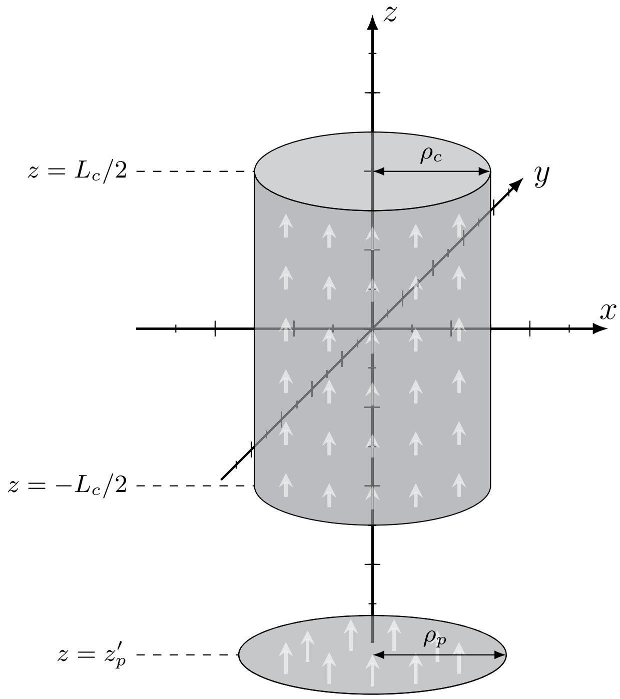

FIG. 1. Schematic diagram of the magnetization surfaces: a cylinder of radius ρ_c and length L_c and a circular plane of radius ρ_p that lies at axial position z_p. White arrows denote the case where the surfaces are axially magnetized along the $+\hat{\mathbf{z}}$ direction.

formulation such that the magnetic scalar potential can be determined simply. Then, by expressing the axial magnetization in terms of mutually orthogonal modes on a surface, the magnetic field can be similarly expressed using corresponding modes that are mutually orthogonal across all of space.

B. Cylindrical surface

Let us examine axial magnetization bound to an infinitesimally thin cylinder of radius ρ_c and length L_c, centered about the origin, as presented in the upper section of Fig. 1. We can represent the axial magnetization in cylindrical coordinates as

$$M_z = \delta(\rho' - \rho_c)\sigma_{zc}(\phi', z'), \tag{7}$$

where $\sigma_{zc}(\phi', z')$ is the axial surface magnetization, i.e., the magnetic dipole moment density per unit area on the cylindrical surface.

Now, we apply a Green's function with simple cylindrical symmetries [35]

$$\frac{1}{|\mathbf{r} - \mathbf{r}'|} = \frac{1}{\pi} \sum_{m=-\infty}^{\infty} e^{im(\phi-\phi')} \times \int_{-\infty}^{\infty} \mathrm{d}k\, e^{ik(z-z')} I_m(|k|\rho_<) K_m(|k|\rho_>), \tag{8}$$

and examine the magnetic field inside the surface magnetization, i.e., $\rho_< = \rho$ and $\rho_> = \rho'$. Substituting Eqs. (8) and (7) into Eq. (5) and then integrating over the radial coordinate, we find that

$$\Psi(\rho, \phi, z) = -\frac{i\rho_c}{2\pi} \sum_{m=-\infty}^{\infty} e^{im\phi} \times \int_{\infty}^{\infty} \mathrm{d}k\, k I_m(|k|\rho) K_m(|k|\rho_c) e^{ikz} \sigma_{zc}^m(k), \tag{9}$$

where the Fourier transform of the axial magnetization on the cylindrical surface is

$$\sigma_{zc}^m(k) = \frac{1}{2\pi} \int_0^{2\pi} \mathrm{d}\phi' e^{-im\phi'} \int_{-\infty}^{\infty} \mathrm{d}z'\, e^{-ikz'} \sigma_{zc}(\phi', z'). \tag{10}$$

Thus, the magnetic flux density, expressed in cylindrical coordinates, $\mathbf{B} = B_\rho\, \hat{\boldsymbol{\rho}} + B_\phi\, \hat{\boldsymbol{\phi}} + B_z\, \hat{\mathbf{z}}$, may be formulated by calculating the gradient of the scalar potential, using Eq. (1), with vector components

$$B_\rho(\rho, \phi, z) = -\frac{i\mu_0\rho_c}{2\pi} \sum_{m=-\infty}^{\infty} e^{im\phi} \times \int_{\infty}^{\infty} \mathrm{d}k\, k|k| I'_m(|k|\rho) K_m(|k|\rho_c) e^{ikz} \sigma_{zc}^m(k), \tag{11}$$

$$B_\phi(\rho, \phi, z) = \frac{\mu_0\rho_c}{2\pi\rho} \sum_{m=-\infty}^{\infty} m e^{im\phi} \times \int_{\infty}^{\infty} \mathrm{d}k\, k I_m(|k|\rho) K_m(|k|\rho_c) e^{ikz} \sigma_{zc}^m(k), \tag{12}$$

$$B_z(\rho, \phi, z) = \frac{\mu_0\rho_c}{2\pi} \sum_{m=-\infty}^{\infty} e^{im\phi} \times \int_{\infty}^{\infty} \mathrm{d}k\, k^2 I_m(|k|\rho) K_m(|k|\rho_c) e^{ikz} \sigma_{zc}^m(k). \tag{13}$$

The magnetic flux density can then be evaluated by calculating the Fourier transform of the axial surface magnetization and approximating the Fourier space integrals numerically.

Now, let us return to our magnetized cylinder of radius ρ_c and length L_c and impose a complete basis of orthogonal modes bound to its surface. This is best expressed using a

Fourier series,

$$\sigma_{zc}(\phi', z') = \mathcal{T}\left(z', -\frac{L_c}{2}, \frac{L_c}{2}\right) \times \sum_{n=1}^{N}\left[W_{n0} + \sum_{m=1}^{M}[W_{nm}\cos(m\phi') + Q_{nm}\sin(m\phi')]\right] \times \sin\left(\frac{n\pi(z' - L_c/2)}{L_c}\right) \tag{14}$$

with the top-hat operator, $\mathcal{T}(x, y, z)$, acting to bound the axial magnetization to the cylindrical surface,

$$\mathcal{T}(x, y, z) = \mathcal{H}(x - y) - \mathcal{H}(x - z), \tag{15}$$

where $\mathcal{H}(x)$ is the Heaviside step function. The symbols (W_{n0}, W_{nm}, Q_{nm}) denote the weightings of the Fourier modes, hereby referred to as *Fourier coefficients*. This basis is encoded such that the axial surface magnetization smoothly tends to zero at the axial edge of the cylinder to make the magnet easier to construct.

Substituting Eq. (14) into Eqs. (11)–(13), we generate the governing equations

$$B_\rho(\rho, \phi, z) = \sum_{n=1}^{N}\left[W_{n0}B^{n0}_{\rho,c/p}(\rho, z) + \sum_{m=1}^{M}[W_{nm}\cos(m\phi) + Q_{nm}\sin(m\phi)]B^{nm}_{\rho,c/p}(\rho, z)\right], \tag{16}$$

$$B_\phi(\rho, \phi, z) = \sum_{n=1}^{N}\sum_{m=1}^{M}[-W_{nm}\sin(m\phi) + Q_{nm}\cos(m\phi)]B^{nm}_{\phi,c/p}(\rho, z), \tag{17}$$

$$B_z(\rho, \phi, z) = \sum_{n=1}^{N}\left[W_{n0}B^{n0}_{z,c/p}(\rho, z) + \sum_{m=1}^{M}[W_{nm}\cos(m\phi) + Q_{nm}\sin(m\phi)]B^{nm}_{z,c/p}(\rho, z)\right], \tag{18}$$

where $(B^{nm}_{\rho,c/p}, B^{nm}_{\phi,c/p}, B^{nm}_{z,c/p})$ represent the governing integrals that weight the Fourier coefficients with the subscripts c and p denoting the cylindrical and circular-planar cases, respectively (see Sec. II C below). In the cylindrical case, these governing integrals are

$$B^{nm}_{\rho,c}(\rho, z) = 2n\mu_0\rho_c L_c \int_0^\infty \mathrm{d}k \times \frac{k^2 I'_m(k\rho)K_m(k\rho_c)}{n^2\pi^2 - L_c^2k^2}\begin{Bmatrix}\sin(kz)\cos(kL_c/2)\\ -\cos(kz)\sin(kL_c/2)\end{Bmatrix}, \tag{19}$$

$$B^{nm}_{\phi,c}(\rho, z) = \frac{2nm\mu_0\rho_c L_c}{\rho}\int_0^\infty \mathrm{d}k \times \frac{kI_m(k\rho)K_m(k\rho_c)}{n^2\pi^2 - L_c^2k^2}\begin{Bmatrix}\sin(kz)\cos(kL_c/2)\\ -\cos(kz)\sin(kL_c/2)\end{Bmatrix}, \tag{20}$$

$$B^{nm}_{z,c}(\rho, z) = 2n\mu_0\rho_c L_c \int_0^\infty \mathrm{d}k \times \frac{k^2 I_m(k\rho)K_m(k\rho_c)}{n^2\pi^2 - L_c^2k^2}\begin{Bmatrix}\cos(kz)\cos(kL_c/2)\\ \sin(kz)\sin(kL_c/2)\end{Bmatrix}, \tag{21}$$

where the vector $\{2n - 1, 2n\}$ denotes the magnetic flux density for either odd, $2n - 1$, or even, $2n$, orders for $n \in \mathbb{Z}^+$.

These integrals can be approximated numerically to determine the magnitude of the field generated by each axial surface magnetization mode at each point in space. During numerical approximation, the high spatial frequency limit, $k \to \infty$, in the integrands may be approximated as a large number, as determined by the spatial frequency of the oscillations (see the example in Sec. III below). Designs on a larger geometry oscillate more at a given spatial frequency and so the integrals converge faster.

C. Circular-planar surface

Now, let us examine the magnetic field above or below a source of axial magnetization bound to a circular ρ-ϕ plane of radius ρ_p at axial position $z' = z_p$, as presented in the lower section of Fig. 1. We express this surface magnetization as

$$M_z = \delta(z' - z_p)\sigma_{zp}(\rho', \phi'), \tag{22}$$

where $\sigma_{zp}(\rho', \phi')$ is the axial surface magnetization bound to the circular plane.

To exploit the radial symmetries in this system, we apply a Green's function in cylindrical coordinates defined in terms of Bessel functions of the first kind [35],

$$G(\mathbf{r}, \mathbf{r}') = \sum_{m=-\infty}^{\infty} e^{im(\phi-\phi')} \times \int_0^\infty \mathrm{d}k\, e^{-k|z-z'|}J_m(k\rho)J_m(k\rho'). \tag{23}$$

Substituting Eq. (23) into Eq. (5), and then integrating over the axial coordinate, we find that

$$\Psi(\rho,\phi,z) = \frac{1}{2}\frac{(z-z_p)}{|z-z_p|} \times \sum_{m=-\infty}^{\infty} e^{im\phi}\int_0^\infty \mathrm{d}k\, k e^{-k|z-z_p|}J_m(k\rho)\sigma_{zp}^m(k). \tag{24}$$

Here, we define $\sigma_{zp}^m(k)$ as the cylindrical Fourier transform of the axial surface magnetization,

$$\sigma_{zp}^m(k) = \frac{1}{2\pi}\int_0^\infty d\rho'\rho'\int_0^{2\pi}\mathrm{d}\phi'\, e^{-im\phi'}J_m(k\rho')\sigma_{zp}(\rho',\phi'). \tag{25}$$

Equation (25) is sometimes referred to as the Hankel transform of the mth order. Substituting Eq. (24) into Eq. (1), the magnetic flux density vector components are

$$B_\rho(\rho,\phi,z) = \frac{\mu_0}{2}\frac{z-z_p}{|z-z_p|}\sum_{m=-\infty}^{\infty} e^{im\phi} \times \int_0^\infty \mathrm{d}k\, k^2 e^{-k|z-z_p|}J_m'(k\rho)\sigma_{zp}^m(k), \tag{26}$$

$$B_\phi(\rho,\phi,z) = \frac{i\mu_0}{2\rho}\frac{z-z_p}{|z-z_p|}\sum_{m=-\infty}^{\infty} m e^{im\phi} \times \int_0^\infty \mathrm{d}k\, k e^{-k|z-z_p|}J_m(k\rho)\sigma_{zp}^m(k), \tag{27}$$

$$B_z(\rho,\phi,z) = -\frac{\mu_0}{2}\sum_{m=-\infty}^{\infty} e^{im\phi} \times \int_0^\infty \mathrm{d}k\, k^2 e^{-k|z-z_p|}J_m(k\rho)\sigma_{zp}^m(k). \tag{28}$$

A complete basis of orthogonal modes on a circular surface can be expressed in terms of a Fourier-Bessel series, which is the discrete counterpart of the Hankel transform. Thus, we represent the axial surface magnetization bound to the circular plane as

$$\sigma_{zp}(\rho',\phi') = \mathcal{T}(\rho',0,\rho_p)\sum_{n=1}^{N}\left[W_{n0}J_0\left(\frac{\varrho_{n0}\rho'}{\rho_p}\right) + \sum_{m=1}^{M}[W_{nm}\cos(m\phi') + Q_{nm}\sin(m\phi')] \times J_m\left(\frac{\varrho_{nm}\rho'}{\rho_p}\right)\right], \tag{29}$$

where ϱ_{nm} is the nth zero of the Bessel function of the first kind of order m such that $J_m(\varrho_{nm}) = 0$.

Substituting Eq. (29) into Eqs. (26)–(28) and integrating over the surface of the magnet, we find that the governing equations are of the same form as Eqs. (16)–(18) with new integral weightings:

$$B_{\rho,p}^{nm}(\rho,z) = \frac{\mu_0\varrho_{nm}\rho_p^2 J_m'(\varrho_{nm})}{2}\frac{z-z_p}{|z-z_p|} \times \int_0^\infty \mathrm{d}k\, \frac{k^2 J_m'(k\rho)J_m(k\rho_p)e^{-k|z-z_p|}}{\varrho_{nm}^2 - k^2\rho_p^2}, \tag{30}$$

$$B_{\phi,p}^{nm}(\rho,z) = \frac{\mu_0 m\varrho_{nm}\rho_p^2 J_m'(\varrho_{nm})}{2\rho}\frac{z-z_p}{|z-z_p|} \times \int_0^\infty \mathrm{d}k\, \frac{k J_m(k\rho)J_m(k\rho_p)e^{-k|z-z_p|}}{\varrho_{nm}^2 - k^2\rho_p^2}, \tag{31}$$

$$B_{z,p}^{nm}(\rho,z) = -\frac{\mu_0\varrho_{nm}\rho_p^2 J_m'(\varrho_{nm})}{2} \times \int_0^\infty \mathrm{d}k\, \frac{k^2 J_m(k\rho)J_m(k\rho_p)e^{-k|z-z_p|}}{\varrho_{nm}^2 - k^2\rho_p^2}. \tag{32}$$

When designing surface magnetization on multiple coaxial circular planes, we assume that their Fourier modes are spatially orthogonal and adjust the radius and axial position in Eqs. (30)–(32) based on the geometry of each plane.

D. Optimization

Now, we use the target integrals, Eqs. (19)–(21) and (30)–(32) in the cylindrical and circular-planar cases, respectively, to determine the optimal Fourier coefficients, (W_{n0}, W_{nm}, Q_{nm}), to generate a target magnetic field profile. Here, for simplicity and computational speed, we implement this using least-squares optimization of a quadratic cost function; however, other more sophisticated techniques may be applied to the same objective integrals, including linear optimization with inequality constraints [36,37].

Let us pose a quadratic cost function,

$$f(W_n, W_{nm}, Q_{nm}) = \sum_{k}^{N^{\text{target}}} \Delta\mathbf{B}(\mathbf{r}_k)^2 + \beta C, \tag{33}$$

which is determined by the square of the deviation,

$$\Delta\mathbf{B}(\mathbf{r}) = \mathbf{B}^{\text{target}}(\mathbf{r}) - \mathbf{B}(W_n, W_{nm}, Q_{nm}; \mathbf{r}), \tag{34}$$

of the modal magnetic flux density from a target, $\mathbf{B}^{\text{target}}(\mathbf{r})$, evaluated at $k \in [1, N^{\text{target}}]$ points within a target-field region.

The cost function in Eq. (33) includes a regularization parameter, C, weighted by a parameter β, that is quadratic with respect to the Fourier coefficients. Here, we set the regularization to be the curvature of the axial surface magnetization,

$$C = \int_{r'} \mathrm{d}^2\mathbf{r}' \, |\nabla^2 M_z(\mathbf{r}')|^2. \tag{35}$$

We choose to regularize using curvature because it relates closely to how easy it is to manufacture the designs. This means that we can control design manufacturability with respect to magnetic field quality by changing the regularization parameter and recalculating the Fourier coefficients. Substituting the cylindrical axial surface magnetization (14) into Eq. (35), calculating its Laplacian, and then integrating over the surface of the cylinder, we find that the curvature of the cylindrical surface magnetization is

$$C = \pi \rho_c L_c \sum_{n=1}^{N} \left[\frac{n^4\pi^4}{L_c^4} W_{n0}^2 + \frac{1}{2} \sum_{m=1}^{M} \left(\frac{m^2}{\rho_c^2} + \frac{n^2\pi^2}{L_c^2} \right)^2 (W_{nm}^2 + Q_{nm}^2) \right]. \tag{36}$$

Following the same approach, we find that the curvature of the circular-planar surface magnetization (29) is

$$C = \frac{1}{2\rho_p^2} \sum_{n=1}^{N} \left[2\varrho_{n0}^4 J_0'(\varrho_{n0})^2 W_{n0}^2 + \sum_{m=1}^{M} \varrho_{nm}^4 J_m'(\varrho_{nm})^2 (W_{nm}^2 + Q_{nm}^2) \right]. \tag{37}$$

The optimization proceeds by finding values of Fourier coefficients that make the derivative of the cost function (33), with respect to the Fourier coefficients, equal to zero [38],

$$\frac{\partial f}{\partial W_{i0}} = 0, \qquad \frac{\partial f}{\partial W_{ij}} = 0, \qquad \frac{\partial f}{\partial Q_{ij}} = 0. \tag{38}$$

These Fourier coefficients minimize deviations from the target-field across the target points as well as the curvature of the axial magnetization. We can then adjust the number and locations of the target points and the weighting of the regularization to determine the best possible design for a given scenario.

E. Surface pattern discretization

After determining the optimal Fourier coefficients via least-squares optimization, we substitute them into Eq. (14) [cylinder] or (29) [circular plane] to calculate the optimal surface magnetization patterns. The resulting optimal patterns feature continuously varying magnetization across their surfaces, which could be challenging to manufacture. To address this, we now demonstrate a process for approximating the surface magnetization at a set of discrete values, where each continuous value is substituted with its closest discrete counterpart.

Let us demonstrate this approach for the cylindrical case. We evaluate an odd number of equally spaced domain levels, $N^{\text{disc.}} = 2n + 1$ for $n \in \mathbb{Z}^+$, and assume that all surface magnetization within a specific bound of each level is equal to the value at its center point. The domain levels are centered at discrete axial surface magnetization values

$$\sigma_{zc}^{\text{disc.}} = n^{\text{disc.}} \Delta_{zc}^{\text{disc.}}, \tag{39}$$

where the span of each domain level is

$$\Delta_{zc}^{\text{disc.}} = \max(2|\sigma_{zc}|)/N^{\text{disc.}}. \tag{40}$$

Each discrete level encompasses all the continuous values between $\sigma_{zc} = \sigma_{zc}^{\text{disc.}} + [-\Delta_{zc}^{\text{disc.}}/2, \Delta_{zc}^{\text{disc.}}/2]$. The level indices are evenly distributed half-integers,

$$n^{\text{disc.}} = [-N^{\text{disc.}}/2 + 1/2, -N^{\text{disc.}}/2 + 3/2, \ldots, N^{\text{disc.}}/2 - 3/2, N^{\text{disc.}}/2 - 1/2]. \tag{41}$$

An example of this process for a single Fourier mode is illustrated in Fig. 2. Unlike contouring approaches typically used in magnetic field coil design [39], the domains are evenly distributed around the origin with one level always set at $\sigma_{zc}^{\text{disc.}} = 0$, where no magnetic material is present [see the white zero level in Fig. 2(c)]. This ensures that the discrete pattern can be represented by expanding the 2D surface into a thin 3D volume with incrementally varying thickness.

In the varying thickness scenario, instead of an infinitely thin cylinder, the magnetization can be approximated as being distributed on a thin cylindrical tube centered at radial distance ρ_c with a fixed axial magnetization M_{0z} and a small radial thickness $\rho_{c0} \ll \rho_c$. The radial wall thickness of each domain is now

$$\rho_{c0}^{\text{disc.}} = |n^{\text{disc.}}| \Delta_{zc}^{\text{disc.}} / M_{0z}. \tag{42}$$

The polarity (positive or negative) of the axial magnetization is determined by $\text{sgn}(n^{\text{disc.}})$, where sgn is $+1$ if the argument is positive and -1 if the argument is negative.

As already shown in nuclear magnetic resonance imaging [40], such patterns can be constructed using cylindrical permanently axially magnetized plates of equal thicknesses overlaid on top of one another. Here, the number of plates at each point on the surface would be equal to $|n^{\text{disc.}}|$. If the number of domain levels $N^{\text{disc.}}$ is insufficient or the maximum tube thickness $\max(\rho^{\text{disc.}})$ increases compared to ρ_c, errors may be introduced into the model. This

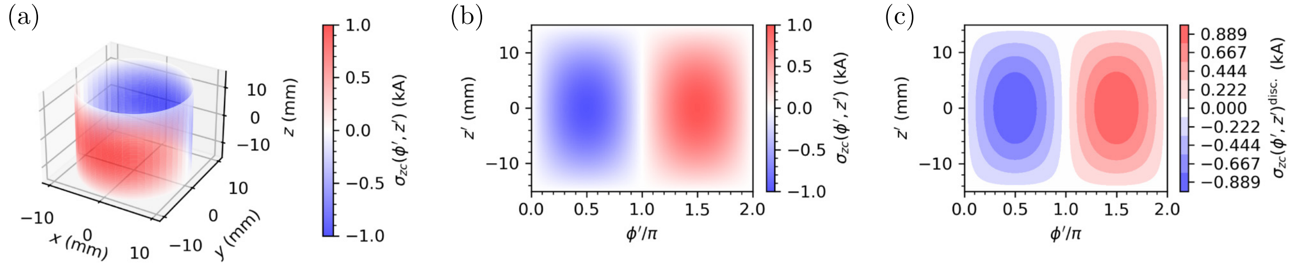

FIG. 2. Axial surface magnetization from Eq. (14), for $Q_{1,1} = 1 \times 10^3$ A and all other Fourier coefficients zero, on a cylindrical surface of radius $\rho_c = 10$ mm and length $L_c = 30$ mm: (a) presented in three dimensions and (b) presented in two dimensions for the surface continuum and in (c) for $N^{\text{disc.}} = 9$ levels. Red (blue) coloring indicates positive (negative) axial magnetization with increased intensity representing greater strength.

can be analyzed *a posteriori*, as demonstrated in Sec. IV below for a simple case study.

This approach can also be applied to the circular-planar example. Instead of extruding the cylinder along the radial direction, we extrude the plane along the axial direction. The approach remains the same, except that the plates are now placed on a circular plane, centered at axial position z_p, with varying axial thickness

$$z_{p0}^{\text{disc.}} = |n^{\text{disc.}}|\Delta_{zp}^{\text{disc.}}/M_{0z}, \tag{43}$$

where

$$\Delta_{zp}^{\text{disc.}} = \max(2|\sigma_{zp}|)/N^{\text{disc.}}. \tag{44}$$

III. RESULTS

Now, we use the mathematical model to design magnetic-field-generating arrangements that generate uniform axial, B_z, and transverse, B_y, magnetic fields. We design four of these arrangements on independent axially magnetized cylinders and circular biplanes.

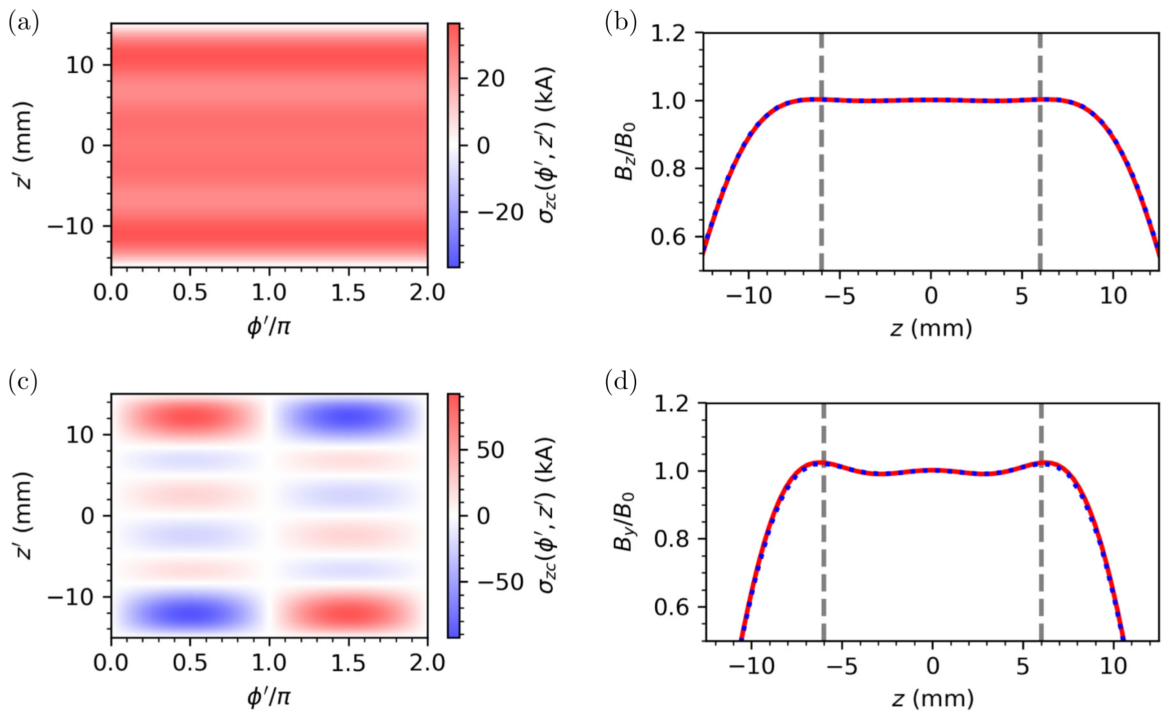

FIG. 3. (a) Axial surface magnetization, σ_{zc}, on a cylinder of radius $\rho_c = 10$ mm and length $L_c = 30$ mm to generate a uniform axial magnetic field, B_z. Red (blue) coloring indicates positive (negative) axial magnetization with increased intensity representing greater strength. (b) Normalized axial magnetic field, B_z/B_0, where $B_0 = 10$ mT, generated by the design in (b) along the z axis calculated from the analytic model (red solid line) and simulated using FEM (blue dotted line), where the cylinder is of thickness $\rho_{c0} = 1$ mm. The edges of the target region are highlighted (dashed gray lines). (c) Axial surface magnetization to generate a uniform transverse magnetic field, B_y [labeled as (a)]. (d) Normalized transverse field along the z axis generated by the design in (c) [labeled as (b)].

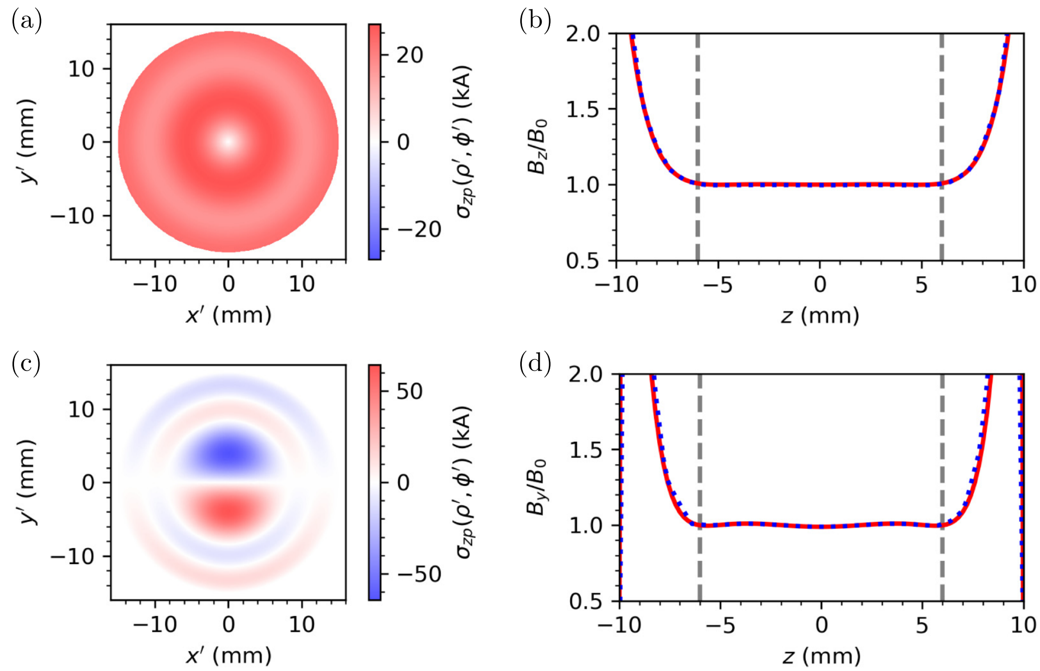

FIG. 4. (a) Axial surface magnetization, σ_{zp}, on the upper circular plane of radius $\rho_p = 15$ mm of an axially magnetized biplanar pair at axial positions $z'_p = \pm 10$ mm. Red (blue) coloring indicates positive (negative) axial magnetization with increased intensity representing greater strength. The magnetization pattern on the lower plane is identical to that on the upper plane. (b) Normalized axial magnetic field, B_z/B_0, where $B_0 = 10$ mT, generated by the pair in (a) along the z axis calculated from the analytic model (red solid line) and simulated using FEM (blue dotted line), where the planes are of thickness $z_{c0} = 1$ mm. The edges of the target region are highlighted (dashed gray lines). (c) Axial surface magnetization to generate a uniform transverse magnetic field, B_y [labeled as (a)], except that the magnetization pattern on the lower plane is equal and opposite to that on the upper plane. (d) Normalized transverse field along the z axis generated by the pair in (c) [labeled as (b)].

Let us first consider a cylindrical surface of radius $\rho_c = 10$ mm and length $L_c = 30$ mm, which is coaxial and cocentered with the origin. In Fig. 3(a), we present an axial surface magnetization pattern designed to generate a uniform axial magnetic field, $B_0 = 10$ mT, within a target region extending over 40% of the cylinder's length, from $z = [-6, 6]$ mm. The pattern is composed of $N = 50$, $M = 0$ Fourier modes with $W_{n,0}$ Fourier coefficients. The governing integrals (19)–(21) converge to an accuracy above one part in 10^6 using a maximum Fourier spatial frequency, $k^{\text{max.}} = 1 \times 10^4$. The integrals are approximated numerically using the `scipy.integrate.quad()` function in PYTHON, taking 20.8 s to compute for all 50 modes at $N^{\text{target}} = 120$ points [41]. The least-squares optimization, performed using `numpy.linalg.lstsq()`, takes less than 0.1 s.

In Fig. 3(b), the axial field generated by this pattern along the z axis, calculated using Eq. (18), is compared to FEM simulations of the axial magnetization, implemented using COMSOL Multiphysics® 6.2a. The simulations approximate the axial surface magnetization as an axial volume magnetization distributed across a cylinder with a thickness of $\rho_{c0} = 1$ mm. The deviations between the analytical model and FEM simulations are minor, within $< 0.05\%$ in the target region, validating the design model. These small discrepancies stem from approximating the surface magnetization as a volume magnetization and FEM meshing limitations. A large mesh resolution helps to account for greater spatial gradients from higher-order modes in Eq. (14). Consequently, the error increases in regions with higher field gradients, such as outside the target region.

In Fig. 3(c), we present an axial surface magnetization pattern designed to generate a uniform B_y field (transverse to the cylinder's axis) on the same cylindrical surface. The resulting transverse magnetic field along the z axis is calculated and compared with FEM simulation results in Fig. 3(d). The agreement between the analytical model and FEM simulations remains within $< 0.05\%$ in the target region. However, the intrinsic uniformity of the transverse field, which exhibits maximum field errors of $< 2\%$ in the target region, is diminished compared to the axial field-generating case above. The field is less uniform because the transverse design requires a more oscillatory surface pattern compared to the axial design [seen when comparing Figs. 3(a) and 3(c) qualitatively]. Even though the resulting design oscillates more, the curvature regularization still needs to be weighted more significantly in the least-squares optimization of the uniform transverse field, which diminishes the magnetic field uniformity.

We now design configurations to generate equivalent magnetic fields using a pair of circular biplanar surfaces instead of cylindrical surfaces. Designing on biplanes is generally preferred when the system's aspect ratio (length to diameter) is less than one [42]. To compare with the cylindrical case, we therefore design arrangements on a pair of axially magnetized circular biplanes with a radius of $\rho_p = 15$ mm, positioned at $z = \pm z_p$, where $z_p = 10$ mm. This setup makes the cylindrical system's aspect ratio the reciprocal of that of the biplanar system. We optimize magnetic field uniformity within the same spatial region as before: the central 12 cm of the z axis.

In Figs. 4(a) and 4(c), we present axial surface magnetization patterns to generate uniform axial and transverse magnetic fields, respectively. The target-fields along the z axis produced by these patterns, calculated analytically and simulated using FEM, are shown in Figs. 4(b) and 4(d). The FEM simulations assume that the axial surface magnetization is uniformly distributed on circular biplanar disks with a thickness of $z_{p0} = 1$ mm. As in the cylindrical cases, the magnetic fields generated agree closely with the target profiles and with each other. Within the target region, errors from perfect uniformity are $< 1\%$, while deviations between analytic and FEM approaches are $< 0.05\%$. These deviations increase when evaluating the magnetic field outside of the target region, particularly near the circular-planar magnets. They also increase in the transverse field-generating case where the surface magnetization oscillates more greatly.

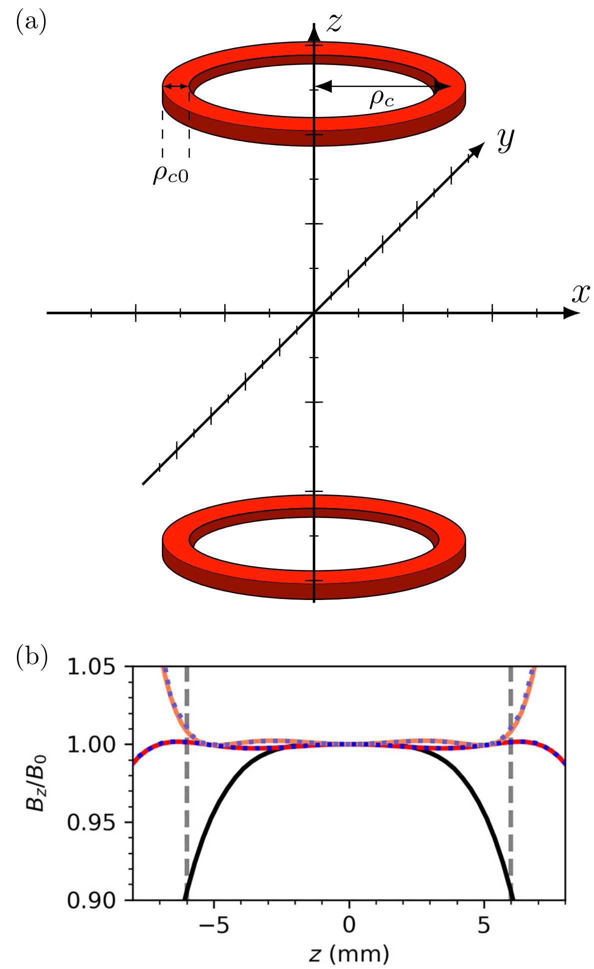

FIG. 5. (a) Schematic diagram of axially symmetric permanent magnet rings of radius $\rho_c = 10$ mm and thickness $\rho_{c0} = 1$ mm at axial positions $z = \pm d_c$, where $d_c = 16.94$ mm (red coloring indicates positive axial magnetization). (b) Normalized axial magnetic field, B_z/B_0, along the z axis calculated for the arrangement in (a) (black solid) alongside the analytical and FEM results in Figs. 3(b) and 4(b), respectively [darker (lighter) shading for the cylindrical (circular) biplanar case].

IV. ANALYSIS

A. Comparison to Helmholtz magnets

Now, we examine the intrinsic performance of designs developed using this methodology compared to standard equivalents and examine limitations on the realization of these designs. Here, we perform this analysis for the uniform axial field-generating designs presented in Sec. III, although the same process could be performed for any magnet design. An additional comparison between the cylindrical uniform transverse field-generating design and a cylindrical Halbach array [43] is presented in the Appendix.

In Fig. 5(a), we show a standard arrangement for generating a uniform axial magnetic field using a pair of axially magnetized loops. The loops have identical magnetization and are positioned at axial locations $z_c = \pm 1.694\rho_c$. The determination of this best separation follows Roméo and Hoult's [24] approach, whereby the uniform field is generated by nulling the leading-order error. In this case, this error is the quadratic gradient of the axial field with respect to the axial position, $\partial^2 B_z/\partial z^2$. This gradient has a magnitude proportional to that of the fourth-order Legendre polynomial, which has a root at $P_{4,0}(x = 1.694) \approx 0$ [44].

In Fig. 5(b), we use FEM simulations to analyze the axial magnetic field produced by this arrangement, where the loops are three-dimensional rings with radius $\rho_c = 10$ mm and thickness $\rho_{c0} = 1$ mm. We compare these results to those generated by the surface magnetization designs in Figs. 3(a) and 4(a). The surface-based designs clearly provide significantly improved magnetic field uniformity compared to the standard ring magnet arrangement. Within the target region, the maximum deviation in the axial field generated by the rings is 7.61%, whereas for the cylindrical and circular biplanar systems, the maximum deviations are 0.268% and 0.586%, respectively. The cylindrical system also has a smaller diameter and length than the ring pair, while the biplanar system is much shorter in length. However, the ring system blocks access

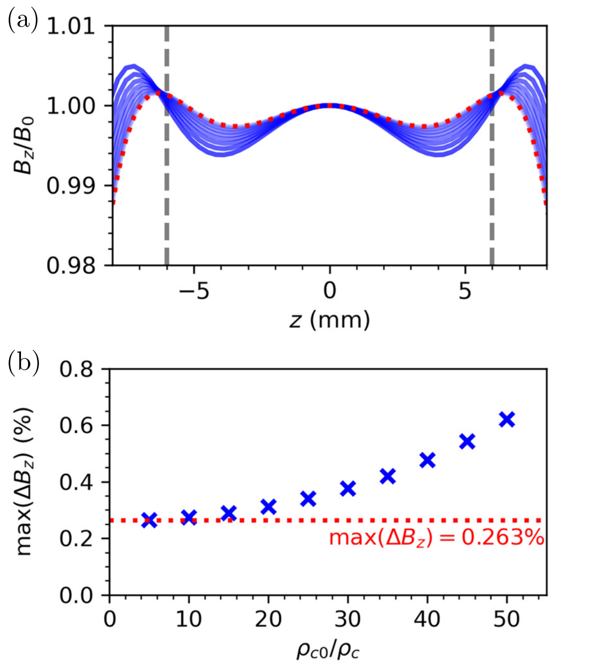

FIG. 6. (a) Normalized axial magnetic field, B_z/B_0, along the z axis calculated from FEM simulations of the arrangement in Fig. 3(a) of radius $\rho_c = 10$ mm, where the thickness of the axially magnetized cylinder, ρ_{c0}, is increased from 0.5 to 5 mm in 0.5 mm increments (light-to-dark blue shading). The red dotted line represents the result in the thin magnet limit, where $\rho_{c0} = 0.1$ mm. The edges of the target region are highlighted (dashed gray lines). (b) Maximum axial magnetic field deviation within the target region, $\max(\Delta B_z)$, as the thickness of the magnetized cylinder increases, with the dotted line representing the deviation in the thin magnet limit.

to a much smaller area and would be significantly easier to construct, and so would still be preferable in settings where these characteristics are critical.

B. Implementation

Next, we use FEM simulations to assess how thick a 3D tube can be while still generating a uniform target axial field, thereby approximating the 2D cylindrical design in Fig. 3(a). Figure 6 examines the effect of varying the thickness of the volume magnetization tube on the generated axial magnetic field and its maximum deviation within the target region. As expected, the axial field varies more as the tube's thickness increases: the maximum deviation increases from 0.263% at the thin magnet limit ($\rho_{c0} = 0.01\rho_c$) to 0.620% for the thickest tube ($\rho_{c0} = 0.5\rho_c$). Despite this increase, the error remains more than an order of magnitude smaller than that of the standard ring magnet arrangement (7.61%), as shown in Fig. 5(b). This shows that even very thick 3D approximations to surface magnetization profiles can perform better than standard designs.

While the acceptable error threshold depends on the specific application and design requirements, a general guideline is to maintain $\rho_{c0} \leq 0.1\rho_c$ for many applications. For the same total magnetization, increasing the thickness does reduce the field magnitude slightly as more volume is located on the cylinder's larger-radius regions. However, this reduction is minor, with the axial field magnitude being only 0.96% lower at $\rho_{c0} = 0.50\rho_c$ compared to the thin magnet limit.

In Fig. 7, we examine how varying the number of discretization levels in the design shown in Fig. 3(a) impacts the maximum magnetic field deviation across the target region. Examples of the discretized patterns at selected discretization levels are presented in Fig. 8. The deviation displays an interesting pattern that offers valuable insight into the design of surface magnets. Initially, the error is approximately 2.5%, as the poorly discretized pattern resembles a uniform axial surface magnetization across the magnet cylinder [Fig. 8(a)]. As the number of levels increases, the error rises because the spatial oscillations

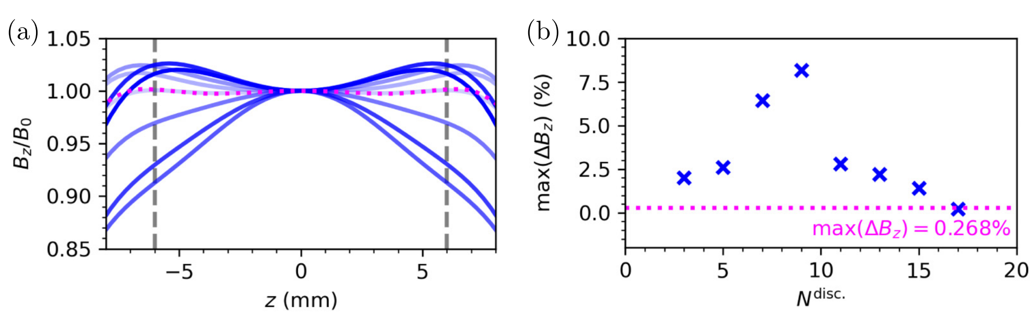

FIG. 7. (a) Normalized axial magnetic field, B_z/B_0, along the z axis calculated from FEM simulations of the arrangement in Fig. 3(a) of radius $\rho_c = 10$ mm and fixed thickness $\rho_{c0} = 1$ mm, where the number of discretization levels, $N^{\text{disc.}}$, is increased from 3 to 17 in odd intervals (dark-to-light blue shading). The magenta dotted line represents the result in the continuum limit. The edges of the target region are highlighted (dashed gray lines). (b) Maximum axial magnetic field deviation within the target region, $\max(\Delta B_z)$, as the number of discretization levels increases, with the dotted line representing the deviation in the continuum limit.

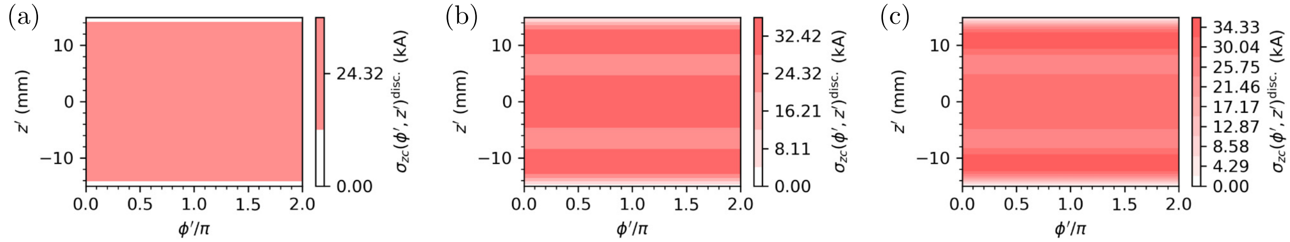

FIG. 8. Axial surface magnetization in Fig. 3(a) on a cylindrical surface of radius $\rho_c = 10$ mm and length $L_c = 30$ mm, presented at (a) $N^{\text{disc.}} = 3$, (b) $N^{\text{disc.}} = 9$, and (c) $N^{\text{disc.}} = 17$ discretization levels. Red coloring indicates positive axial magnetization with increased intensity representing greater strength.

in the surface magnetization pattern are inadequately represented [Fig. 8(b)]. However, when the oscillations are accurately represented with $N^{\text{disc.}} \geq 13$, the error decreases as the discretized pattern captures more detail regarding the design. At $N^{\text{disc.}} = 17$ discretization levels [Fig. 8(c)], the error in the discretized field across the target region drops to 0.210%, which is actually lower than the error intrinsic in the design in the continuum limit, where $N^{\text{disc.}} \to \infty$. Analogous relationships are observed when approximating surface current flows as wires in coil design at a varying number of contour levels, where local minima may offer improved target-field fidelity at a reduced number of contour levels [45,46].

These analyses highlight the need for *a posteriori* examination of each design for a full determination of its characteristics. If this is not possible, as a general rule, designs should allow for as many discretization levels as possible, and the curvature regularization weighting should be increased if the manufacturing method limits the feasible number of discretization levels.

Finally, it is important to consider the coercivity of the magnetic material and the overall field strength in system design. Generally, principles from Halbach array design [47,48] can be applied to the design of surface permanent magnets. Strong fields generated outside or by the system can potentially demagnetize the material. Therefore, the magnet material grade must be selected such that its coercivity is much greater than the maximum field at any point within the magnet. Again, this may be examined using FEM simulations. For example, let us consider the uniform axial field-generating design with $N^{\text{disc.}} = 17$ levels, detailed in Fig. 8(c). If this design was constructed using sintered N38 neodymium [49], the maximum magnetic field strength inside the magnet to generate the strength $B_0 = 10$ mT is $|\mathbf{H}_{\text{int.}}| \approx 500$ kA/m. This is significantly below the approximate 900-kA/m material coercivity of N38 neodymium, and so the magnet would be unsaturated and would perform according to the theoretical model.

V. CONCLUSIONS

In this paper, we presented a method for optimizing magnetization on a 2D surface to generate target magnetic fields. We mathematically described the relationship between axial surface magnetization on cylindrical and circular-planar geometries and the resulting magnetic field. We used this model to design uniform axial and transverse magnetic fields using regularized least-squares optimization. Our model closely matched numerical simulations and the uniform axial field-generating designs are over an order of magnitude more uniform across an equivalent region than the field generated by a simple pair of axially magnetized rings. Our approach assumes a fixed magnetization and, to implement experimentally, may require the 2D magnetization surface to be approximated by a 3D volume. We demonstrated using FEM that an axial field-generating design on a cylinder may be approximated as being housed on a thin tube without diminishing the design performance. We find a rule of thumb that the tube should be about an order-of-magnitude thinner than its radius. Finally, we demonstrated methods to approximate the surface pattern using a discrete number of magnetization values and then examined the resulting discrete magnetization profile *a posteriori* using FEM.

Optimized surface permanent magnets have the potential to enhance performance in various devices and disciplines, from electric machines and transducers to magnetic resonance imaging and fundamental physics. The next stage of this research is experimental validation of the designs produced using this method and then implementation into these settings. Realizing the resulting magnetization profiles experimentally, particularly those that oscillate greatly across their surfaces, may require additive manufacturing such as 3D printing of bonded neodymium magnets [50] and other electromagnetic materials [51]. Alternatively, directly manufacturing a discretized pattern using a stack of equally magnetized plates may be simpler, although a thorough analysis of both 2D-to-3D surface thickness and discretization effects must be performed for any new design to ensure that the significant performance benefits expected from this approach are realized experimentally.

Extensive additional theoretical research may also build on this approach. Future designs may combine both cylindrical and circular-planar surface magnetization to further optimize magnetic field fidelity. Additional theoretical work may explore the target-field design approach for radial or azimuthal surface magnetization, or magnet designs could be encoded to account for the interaction with external magnetic shielding [52–54] for applications requiring strong static magnetic fields with low magnetic noise, such as in biassing ion quantum computers [55].

ACKNOWLEDGMENTS

We acknowledge support from the UK Quantum Technology Hub Sensors and Timing, funded by the Engineering and Physical Sciences Research Council (EP/M013294/1).

We also thank Dr Michael Packer for his enlightening contributions during discussions about magnetic field design.

P.J.H and M.F have a worldwide patent (WO/2021/053356) that includes some magnetic design techniques applied in this work.

APPENDIX: COMPARISON TO A HALBACH ARRAY

Halbach arrays are specific arrangements of magnetization that produce a strong magnetic field on one side of the array while generating zero magnetic field on the opposite side [22]. In this appendix, we compare the transverse field-generating performance of a surface-based design to the cylindrical Halbach array depicted in Fig. 2 of Ref. [43], which is utilized for magnetizing para-hydrogen. A schematic of the design is provided in Fig. 9(a). The design contains five layers of eight transversely magnetized segments to generate a uniform transverse field. The radii and number of stacked plates are selected so that the total inner radius and length of the design is equivalent to the cylindrical transverse field-generating design illustrated in Fig. 3(c).

In Fig. 9(b), we employ FEM simulations to evaluate the transverse magnetic field produced by this Halbach array arrangement and compare it to that generated by the surface magnetization design shown in Fig. 3(c). The surface-based design generates a significantly more uniform magnetic field. Within the target region, the maximum deviation in the transverse field generated by the Halbach design is 3.88%, whereas for the cylindrical system, it is only 1.73%. However, it is important to note that the Halbach design incorporates an additional consideration of minimizing the magnetic field on the exterior, which imposes a constraint on its performance. Future research may involve analytically solving for the magnetic field generated exterior to surface-based magnetization surfaces, enabling the imposition of a zero external magnetic field boundary condition. This approach would be analogous to methods currently used to couple to magnetic shielding in magnetic coil design [52].

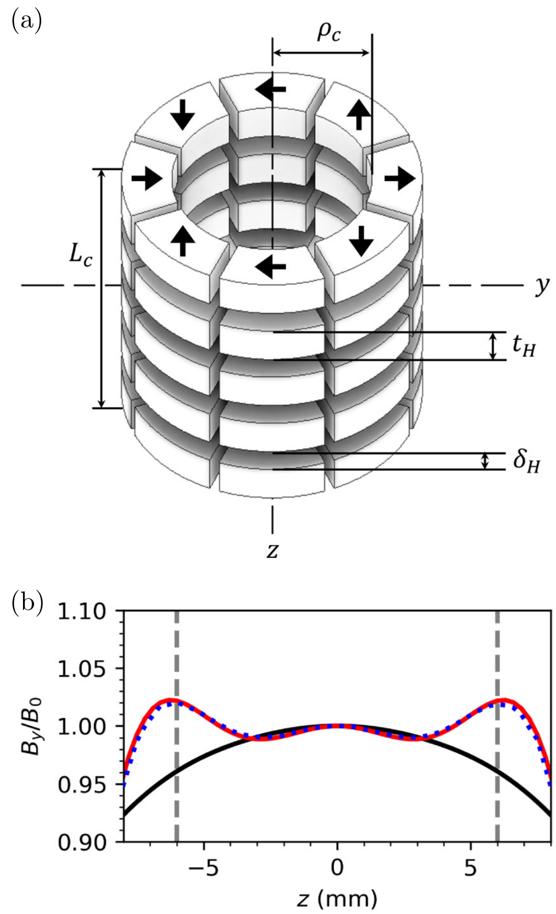

FIG. 9. (a) Schematic diagram of a Halbach array based on that in Ref. [43], with inner radius $\rho_c = 10$ mm and length $L_c = 30$ mm. The magnetized blocks have a height of $t_H = 4$ mm, and are separated by $\Delta_H = 2.5$ mm gaps. Black arrows represent the direction of magnetization of the array along the (transverse) x-y plane. (b) Normalized transverse magnetic field, B_y/B_0, along the z axis calculated for the arrangement in (a) (black solid) alongside analytical and FEM results for an equivalent surface-based design as presented in Fig. 3(d).

[1] J. Gieras, *Permanent Magnet Motor Technology: Design and Applications* (Taylor & Francis CRC Press Group, Boca Raton, Florida, USA, 2010).

[2] S. Zhang, J. Xu, J. Junak, D. Fiederling, G. Sawczuk, M. Koch, A. Schalja, M. Podack, and J. Baumgartner, in *2012 2nd International Electric Drives Production Conference (EDPC)* (IEEE, Nuremberg, Germany, 2012), p. 1.

[3] T. Pham, P. Kwon, and S. Foster, Additive manufacturing and topology optimization of magnetic materials for electrical machines—a review, Energies **14**, 283 (2021).

[4] J. Wang, G. Jewell, and D. Howe, A general framework for the analysis and design of tubular linear permanent magnet machines, IEEE Trans. Magn. **35**, 1986 (1999).

[5] C. McGarry, A. McDonald, and N. Alotaibi, in *2019 IEEE International Electric Machines & Drives Conference (IEMDC)* (IEEE, San Diego, CA, USA, 2019), p. 656.

[6] E. R. Geddes, Transducer flux optimization (1994), US Patent 5343533A, US Patent Office, Alexandria, Virginia, USA.

[7] J. N. Morgan, A. J. Keane, M. B. Harvey, C. D. Pittman, and R. L. Coates, Loudspeaker magnet and earphone assembly (2019), US patent 10469951, US Patent Office, Alexandria, Virginia, USA.

[8] M. Landreman and C. Zhu, Calculation of permanent magnet arrangements for stellarators: A linear least-squares method, Plasma Phys. Contr. Fusion **63**, 035001 (2021).

[9] Z. Lu, G. Xu, D. Chen, X. Zhang, L. Chen, M. Ye, H. Guo, and B. Wan, Development of advanced stellarator with identical permanent magnet blocks, Cell Rep. Phys. Sci. **3**, 100709 (2022).

[10] T. Qian, M. Zarnstorff, D. Bishop, A. Chamblis, A. Dominguez, C. Pagano, D. Patch, and C. Zhu, Simpler optimized stellarators using permanent magnets, Nucl. Fusion **62**, 084001 (2022).

[11] G. Xu, Z. Lu, D. Chen, L. Chen, X. Zhang, X. Wu, M. Ye, and B. Wan, Design of quasi-axisymmetric stellarators with varying-thickness permanent magnets based on Fourier and surface magnetic charges method, Nucl. Fusion **61**, 026025 (2021).

[12] Z. Lu, G. Xu, D. Chen, L. Chen, X. Zhang, M. Ye, and B. Wan, Design of quasi-axisymmetric stellarators with variable-thickness perpendicular permanent magnets based on a two-step magnet design strategy, Nucl. Fusion **61**, 106028 (2021).

[13] J. L. Paulsen, J. Franck, V. Demas, and L.-S. Bouchard, Least squares magnetic-field optimization for portable nuclear magnetic resonance magnet design, IEEE Trans. Magn. **44**, 4582 (2008).

[14] F. Florio, G. Sinha, and R. Sundararaman, Designing high-accuracy permanent magnets for low-power magnetic resonance imaging, IEEE Trans. Magn. **54**, 1 (2018).

[15] A. Parsagian and M. Kleinert, Designing and building a permanent magnet Zeeman slower for calcium atoms using a 3D printer, Am. J. Phys. **83**, 892 (2015).

[16] P. Cheiney, O. Carraz, D. Bartoszek-Bober, S. Faure, F. Vermersch, C. Fabre, G. L. Gattobigio, T. Lahaye, D. guéry odelin, and R. Mathevet, A Zeeman slower design with permanent magnets in a Halbach configuration, Rev. Sci. Instrum. **82**, 063115 (2011).

[17] T. Isoardi, A. Ferretti, L. Bonmassar, and P. Manassero, Modeling and simulation of sputter-ion pump performances, Vacuum **209**, 111792 (2023).

[18] G. H. Lee and H. R. Kim, Numerical analysis of the electromagnetic force for design optimization of a rectangular direct current electromagnetic pump, Nucl. Eng. Technol. **50**, 869 (2018).

[19] S. Madkhaly, L. Coles, C. Morley, C. Colquhoun, T. Fromhold, N. Cooper, and L. Hackermüller, Performance-optimized components for quantum technologies via additive manufacturing, PRX Quantum **2**, 030326 (2021).

[20] E. P. Furlani, The field analysis and simulation of a permanent-magnet bias-field device for magneto-optic recording, J. Phys. D: Appl. Phys. **30**, 1846 (1997).

[21] Y. Liu, Q. Wu, X. Zhang, J. Liu, W. Huang, Y. Zhou, Z. Jia, Y. Zhai, and L. Sun, Design of a 180° electromagnetic isotope separator with inhomogeneous magnetic field, Nucl. Instrum. Methods Phys. Res. A: Accel., Spectrom., Detect. Assoc. Equip. **1006**, 165428 (2021).

[22] K. Halbach, Design of permanent multipole magnets with oriented rare earth cobalt material, Nucl. Instrum. Methods **169**, 1 (1980).

[23] K. Halbach, Application of permanent magnets in accelerators and electron storage rings (invited), J. Appl. Phys. **57**, 3605 (1984).

[24] F. Roméo and D. I. Hoult, Magnet field profiling: Analysis and correcting coil design, Magn. Reson. Med. **1**, 44 (1984).

[25] Q. Peng, S. McMurry, and J. Coey, Axial magnetic field produced by axially and radially magnetized permanent rings, J. Magn. Magn. Mater. **268**, 165 (2004).

[26] J. Selvaggi, S. Salon, O.-M. Kwon, and M. Chari, Calculating the external magnetic field from permanent magnets in permanent-magnet motors-an alternative method, IEEE Trans. Magn. **40**, 3278 (2004).

[27] R. Schmied, D. Leibfried, R. J. C. Spreeuw, and S. Whitlock, Optimized magnetic lattices for ultracold atomic ensembles, New J. Phys. **12**, 103029 (2010).

[28] S. Noguchi, S. Kim, S. Hahn, and Y. Iwasa, Passive shimming by eliminating spherical harmonics coefficients of all magnetic field components generated by correction iron pieces, IEEE Trans. Magn. **50**, 605 (2014).

[29] R. Turner, A target field approach to optimal coil design, J. Phys. D Appl. Phys. **19**, L147 (1986).

[30] L. K. Forbes and S. Crozier, A novel target-field method for finite-length magnetic resonance shim coils: I. Zonal shims, J. Phys. D: Appl. Phys. **34**, 3447 (2001).

[31] L. K. Forbes and S. Crozier, A novel target-field method for finite-length magnetic resonance shim coils: II. Tesseral shims, J. Phys. D: Appl. Phys. **35**, 839 (2002).

[32] L. K. Forbes and S. Crozier, A novel target-field method for magnetic resonance shim coils: III. Shielded zonal and tesseral coils, J. Phys. D: Appl. Phys. **36**, 68 (2002).

[33] J. W. Carlson, K. A. Derby, K. C. Hawryszko, and M. Weideman, Design and evaluation of shielded gradient coils, Magn. Reson. Med. **26**, 191 (1992).

[34] J. D. Jackson, *Classical Electrodynamics* (Wiley, New York, NY, 1962), p. 156, 1st ed.

[35] A. Cabada, *Green's Functions in the Theory of Ordinary Differential Equations* (Springer Briefs in Mathematics, Springer New York, NY, USA, 2014).

[36] A. J. Mäkinen, R. Zetter, J. Iivanainen, K. C. J. Zevenhoven, L. Parkkonen, and R. J. Ilmoniemi, Magnetic-field modeling with surface currents. Part I. Physical and computational principles of bfieldtools, J. Appl. Phys. **128**, 063906 (2020).

[37] R. Zetter, A. J. Mäkinen, J. Iivanainen, K. C. J. Zevenhoven, R. J. Ilmoniemi, and L. Parkkonen, Magnetic field modeling with surface currents. Part II. Implementation and usage of bfieldtools, J. Appl. Phys. **128**, 063905 (2020).

[38] J. Wolberg, *Data Analysis Using the Method of Least Squares: Extracting the Most Information from Experiments* (Springer Science & Business Media, Berlin, Germany, 2006), p. 1.

[39] H. Lopez, M. Poole, and S. Crozier, Eddy current simulation in thick cylinders of finite length induced by coils of arbitrary geometry, J. Magn. Reson. **207**, 251 (2010).

[40] F. X. Li, J. P. Voccio, M. C. Ahn, S. Hahn, J. Bascuñán, and Y. Iwasa, An analytical approach towards passive ferromagnetic shimming design for a high-resolution NMR magnet, Supercond. Sci. Technol. **28**, 075006 (2015).

[41] Calculations are benchmarked using a *MacBookPro18,2* equipped with a *M1 Max* processor with eight 3228-MHz *performance* cores, two 2064-MHz *efficiency* cores, and 32 GB of 512-bit LPDDR5 SDRAM memory.

[42] M. Packer, P. Hobson, N. Holmes, J. Leggett, P. Glover, M. Brookes, R. Bowtell, and T. Fromhold, Planar coil optimization in a magnetically shielded cylinder, Phys. Rev. Appl. **15**, 064006 (2021).

[43] P. Richardson, S. Jackson, A. Parrott, A. Nordon, S. Duckett, and M. Halse, A simple hand-held magnet array for efficient and reproducible sabre hyperpolarisation using manual sample shaking, Magn. Reson. Chem. **56**, 641 (2017).

[44] Another root exists at $P_{4,0}(x = 0.362) \approx 0$; however, this ring magnet design generates a much smaller region with high uniformity than the more separated design.

[45] C. Bidinosti, I. Kravchuk, and M. Hayden, Active shielding of cylindrical saddle-shaped coils: Application to wire-wound RF coils for very low field NMR and MRI, J. Magn. Reson. (San Diego, Calif. : 1997) **177**, 31 (2005).

[46] M. Limes, E. Foley, T. Kornack, S. Caliga, S. McBride, A. Braun, W. Lee, V. Lucivero, and M. Romalis, Portable magnetometry for detection of biomagnetism in ambient environments, Phys. Rev. Appl. **14**, 011002 (2020).

[47] A. R. Insinga, C. Bahl, R. Bjørk, and A. Smith, Performance of Halbach magnet arrays with finite coercivity, J. Magn. Magn. Mater. **407**, 369 (2016).

[48] R. Bjørk, A. Smith, and C. Bahl, The efficiency and the demagnetization field of a general Halbach cylinder, J. Magn. Magn. Mater. **384**, 128 (2015).

[49] Arnold Magnetic Technologies, N38uh: Sintered neodymium-iron-boron magnets (2017), accessed: 2024-07-21.

[50] L. Li, B. Post, V. Kunc, A. Elliott, and P. Paranthaman, Additive manufacturing of near-net-shape bonded magnets: Prospects and challenges, Scr. Mater. **135**, 100 (2017).

[51] H. Tiismus, A. Kallaste, T. Vaimann, and A. Rassõlkin, State of the art of additively manufactured electromagnetic materials for topology optimized electrical machines, Addit. Manuf. **55**, 102778 (2022).

[52] M. Packer, P. Hobson, N. Holmes, J. Leggett, P. Glover, M. Brookes, R. Bowtell, and T. Fromhold, Optimal inverse design of magnetic field profiles in a magnetically shielded cylinder, Phys. Rev. Appl. **14**, 054004 (2020).

[53] P. J. Hobson, N. Holmes, P. Patel, B. Styles, J. Chalmers, C. Morley, A. Davis, M. Packer, T. X. Smith, S. Raudonyte, D. Holmes, R. Harrison, D. Woolger, D. Sims, M. J. Brookes, R. Bowtell, and M. Fromhold, Benchtop magnetic shielding for benchmarking atomic magnetometers, IEEE. Trans. Instrum. Meas. **72**, 1 (2023).

[54] N. Holmes, M. Rea, J. Chalmers, J. Leggett, L. Edwards, P. Nell, S. Pink, P. Patel, J. Wood, N. Murby, D. Woolger, E. Dawson, C. Mariani, T. Tierney, S. Mellor, G. O'Neill, E. Boto, R. Hill, V. Shah, and R. Bowtell, A lightweight magnetically shielded room with active shielding, Sci. Rep. **12**, 13561 (2022).

[55] S. Jain, T. Sägesser, P. Hrmo, C. Torkzaban, M. Stadler, R. Oswald, C. Axline, A. Bautista-Salvador, C. Ospelkaus, D. Kienzler, and J. Home, Penning micro-trap for quantum computing, Nature **627**, 510 (2024).